Materials Chemistry and Physics 350 (2026) 131803

Contents lists available at ScienceDirect

Materials Chemistry and Physics

journal homepage: www.elsevier.com/locate/matchemphys

Anodic film formation on aluminium alloys: Analysis of defects induced by constituent intermetallic particles

João Victor de Sousa Araujo [a,*], Jinghui Chen [b], Isolda Costa [a], Xiaorong Zhou [b]

[a] *Centro de Ciência e Tecnologia de Materiais, Instituto de Pesquisas Energéticas e Nucleares – IPEN/CNEN, Av. Prof. Prof. Lineu Prestes, 2242, São Paulo, Brazil*
[b] *Corrosion and Protection Centre, Department of Materials, The University of Manchester, Manchester, M13 9PL, UK*

HIGHLIGHTS

- **High-copper-containing IMPs dissolve rapidly and form micrometric cavities.**
- **Low-copper-containing IMPs remain partly embedded in the anodic film.**
- **Defect size and depth correlate with IMP copper content and particle size.**
- **Low-Cu IMPs form highly porous anodic films due to slow oxidation.**

GRAPHICAL ABSTRACT

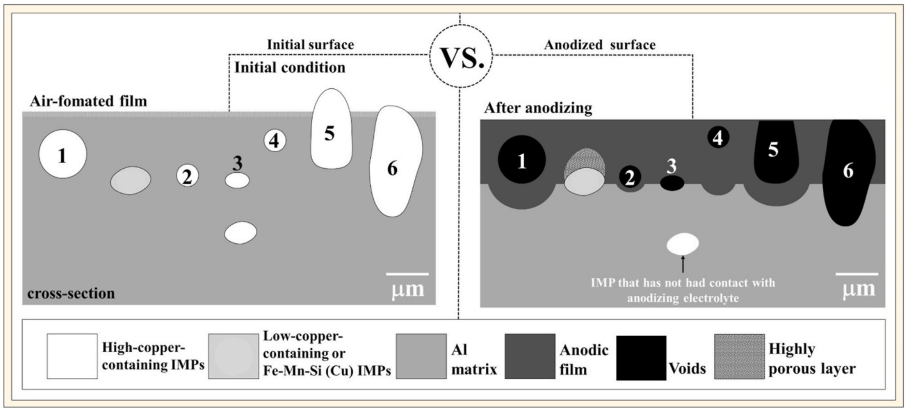

ARTICLE INFO

Keywords:
High-strength aluminium alloys
Anodizing
Constituent intermetallic particles
Defect formation

ABSTRACT

In the present study, anodic film formation on high-strength aluminium alloys (AA2024-T3, AA2198-T8, AA2198-T851 and AA7475-T761) in tartaric–sulfuric acid (TSA) is investigated, with focus on defects induced by the dissolution of constituent intermetallic particles (IMPs) during anodizing. High-copper-containing IMPs dissolve rapidly, generating micrometer-sized cavities in resultant anodic films. In contrast, Fe–Mn–Si (Cu) IMPs in AA2024-T3 and low-copper-containing IMPs in AA7475-T761 exhibit slower dissolution rate than high-copper-containing ones, resulting in locally modified porous morphology and non-uniform film thickness. Further, it is observed that the morphological and compositional uniformity of resultant anodic films are largely affected by the size, location and composition of IMPs.

1. Introduction

Research on the anodizing of aluminium alloys has increasingly focused on the impact of constituent intermetallic particles (IMPs) on anodic film formation [1–25]. Reducing the size or quantity of these IMPs, formed during alloy production, remains technically and

---

* Corresponding author.
E-mail address: jvaraujo@alumni.usp.br (J.V.S. Araujo).

https://doi.org/10.1016/j.matchemphys.2025.131803
Received 5 July 2025; Received in revised form 24 September 2025; Accepted 10 November 2025

economically challenging [26]. Consequently, understanding their behaviour during anodizing has become a key research interest with the aim of minimizing any negative impact on the integrity of anodic film. IMPs typically introduce defects such as discontinuities [27], cavities [28], and localized chemical alterations [29], consequently, compromising the mechanical [30], optical [31], and corrosion-resistant properties of the anodic films [25].

Previous studies [1–4] focused on the anodizing behaviour of IMPs present in AA2024 and AA7050 alloys. These studies demonstrated that IMP dissolution leads to surface defects in anodic films. However, while these investigations provided insights into the behaviour of specific IMPs, they did not comprehensively address the various types of defects that form during anodizing due to the dissolution of IMPs.

Other research focused on aluminium alloys with high silicon content, specifically AA5020 (Al-Mg) [5–7], AA6060 (Al-Mg-Si) [8], and Al–Si foundry alloys [9]. These studies proposed schematic models to describe the behaviour of IMPs during anodizing [10]. However, the alloy-specific nature of these studies limits the broader applicability of their findings to complex aerospace-grade materials.

Studies on AA2024 (Al–Cu–Mg) and AA2198 (Al–Cu–Li) alloys showed that the complete dissolution of IMPs led to defect formation within anodic films [11]. However, these analyses were predominantly limited to surface defects on the anodic film, with little attention given to how these defects manifest throughout film structure. In contrast, work on Al–Cu–Li alloys AA2099 [12–15] and AA2050 [16] revealed the formation of micrometer-sized cavities within anodic films, although these studies primarily addressed corrosion resistance rather than providing detailed classifications of defect types or morphologies.

Research on 7XXX series alloys [17–22] has demonstrated that the defects formed in anodic films are directly influenced by the size and composition of the IMPs, impacting film properties. Nonetheless, a systematic classification of these defects remains absent, hindering a comprehensive understanding of their impact on anodized alloy performance.

Aspects concerning corrosion resistance [32] and mechanical properties [33] of anodic films have recently been explored. While these studies contributed to the understanding of post-anodizing performance, they did not thoroughly explore the influence of IMPs on defect formation and the structural integrity of anodic films. Recently, Araujo et al. [34] demonstrated that IMP-related defects compromise corrosion resistance. However, this work did not classify the defect types or explore the mechanisms underlying their formation. As such, a critical gap persists regarding the correlation between IMP characteristics and the development of local defects, a key factor for predicting the long-term durability of anodic films.

Therefore, a systematic classification of defects induced by IMPs during anodizing of high-strength aluminium alloys is essential. The present study investigates the formation of defects in commercial aluminium alloys (AA2024-T3, AA2198-T8, AA2198-T851, and AA7475-T761) during anodizing, with a focus on classifying defects both, on film surface and within film. By comparing the selected alloys, this study will provide critical insights into how these variables affect the formation of anodic films.

Ultimately, this work aims to answer the following question: How do the chemical composition, size, and spatial distribution of IMPs influence the formation and integrity of anodic films?

2. Experimental

This work investigates the anodizing behaviour of four commercially available aluminium alloys: AA2024-T3 (Al–Cu–Mg), AA2198-T8 and T851 (Al–Cu–Li), and AA7475-T761 (Al–Zn–Mg). These alloys undergo different thermal and mechanical treatments, including solution heat treatment, cold working, and aging. In particular, AA2198-T851 includes an additional stretching step, while AA7475-T761 undergoes stress-relieving. The elemental compositions of the alloys were analyzed using inductively coupled plasma optical emission spectroscopy (ICP-OES), as detailed in Table 1.

For all experiments, the specimens were mechanically ground using P800, P1200, P2400, and P4000 grit silicon carbide papers, followed by sequential polishing with 3 μm and 1 μm diamond suspension. After polishing, they were thoroughly rinsed with deionized water and dried with cold air.

Anodizing was carried out in a tartaric-sulfuric acid (TSA) electrolyte [36] containing 0.46 mol L^{-1} sulfuric acid and 0.53 mol L^{-1} tartaric acid, maintained at 37 ± 1 °C under continuous stirring using a magnetic stirrer. Each sample had an exposed surface area of 1 cm^2, with a platinum mesh (6 cm × 10 cm) as the counter electrode. A constant voltage of 14 V was applied for 20 min. The conditions are similar to that used in the aerospace industry [25].

Sample preparation for cross-sectional analysis involved two techniques: mechanical bending [37,38] and ultramicrotomy [27]. In the bending method, a notch was introduced on the back of the specimen, which was then carefully bent using pliers to expose a clean cross-section while ensuring the anodized film remained outside the bending zone. For ultramicrotomy, thin cross-sections were prepared using a Leica Ultracut instrument with a diamond knife.

Surface characterization was performed using atomic force microscopy (AFM) and scanning electron microscopy (SEM). AFM analyses, used exclusively for surface examination, were conducted with a Nanoscope IIIa multimode microscope in tapping mode, with measurements taken at room temperature under 30–55 % relative humidity. Data was processed using NanoScope Analysis® 1.5 software to evaluate surface topography before and after anodizing. SEM imaging was used for both surface and cross-sectional analysis. A Quanta 650 microscope, operating at 20 kV and equipped with an energy-dispersive X-ray spectroscopy (EDX) system, was employed for compositional analysis, while a Zeiss Ultra 55 microscope at 1.5 kV provided high-resolution cross-sectional images.

3. Results

3.1. Anodizing behaviour of constituent intermetallic particles (IMPs): surface analysis

Fig. 1 presents scanning electron micrographs of the studied aluminum alloys.

Fig. 1 (a1–d1) shows the mechanically polished surfaces of the alloys

Table 1
– Chemical composition of the alloys (wt%) obtained by inductively coupled plasma optical emission spectrometry (ICP-OES).

Elements	Aluminium alloys			
	2024-T3	2198-T8	2198-T851	7475-T761
Al	Balance			
Cu	4.8 (3.8–4.9)	3.34 (2.9–3.5)	3.31 (2.9–3.5)	1.52 (1.2–1.9)
Mg	0.59 (1.2–1.8)	0.31 (0.25–0.80)	0.31 (0.25–0.80)	1.8 (1.9–2.6)
Mn	0.52 (0.3–0.9)	0.003 (≤ 0.50)	0.003 (≤ 0.50)	0.05 (≤0.06)
Li	–	0.95 (0.81–1.1)	0.96 (0.81–1.1)	–
Fe	0.18 (≤ 0.5)	0.04 (≤ 0.10)	0.04 (≤ 0.10)	0.07 (≤ 0.12)
Zn	0.11 (≤ 0.25)	0.006 (≤ 0.35)	0.006 (≤ 0.35)	6.10 (5.2–6.2)
Si	0.07 (≤ 0.5)	0.04 (≤ 0.08)	0.03 (≤ 0.08)	0.03 (≤ 0.06)
Zr	–	0.05 (0.04–0.18)	0.05 (0.04–0.18)	–
Ag	–	0.26 (0.2–0.3)	0.25 (0.2–0.3)	–
Cr	–	–		0.20 (0.18–0.25)

Note: Values in parentheses present the composition specification according to ASM [35] for the aluminium alloys.

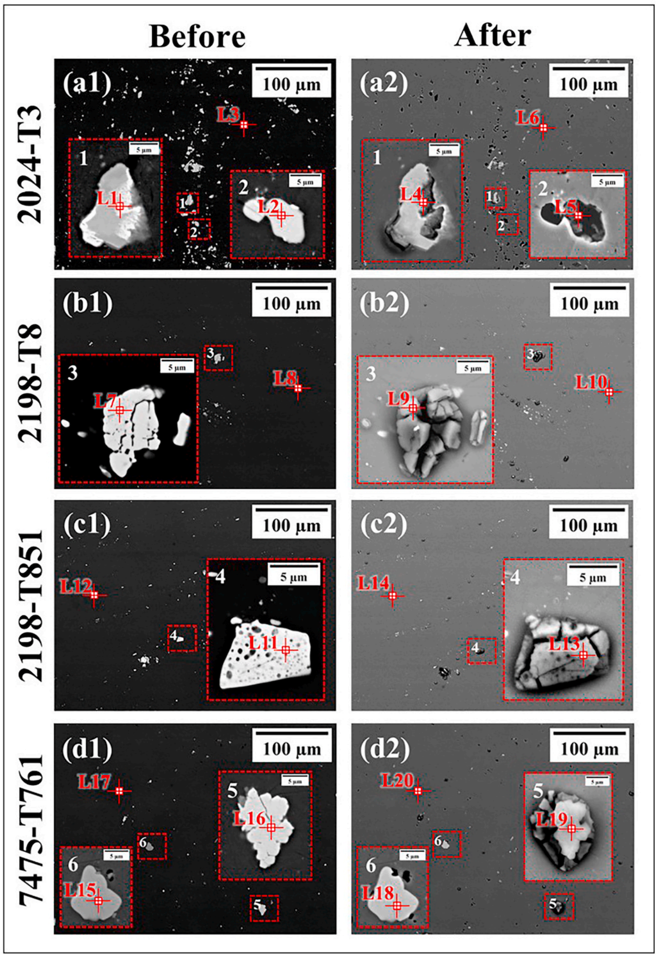

Fig. 1. – Scanning electron micrographs of aluminium alloys at lower magnification, before (a1–d1) and after (a2–d2) anodizing for 5 s. The red dashed squares (1–5) indicate higher magnification regions containing constituent intermetallic particles (IMPs) before and after anodizing. All images were acquired in backscattered electron (BSE) mode at an accelerating voltage of 20 kV. (For interpretation of the references to colour in this figure legend, the reader is referred to the Web version of this article.)

before anodizing, highlighting the presence of IMPs, which appear as bright regions due to their higher atomic number. The dashed square regions (1–6) indicate higher-magnification areas, allowing for a detailed analysis of these particles before and after anodizing. After 5 s of anodizing, the corresponding images in Fig. 1 (a2–d2) reveal morphological changes in the IMPs.

The composition of the alloy matrix and IMPs, both before and after anodizing, was determined using EDX analysis, as presented in Table 2. The measurements were taken at specific locations (L1–L20 in Fig. 1), covering both the matrix and the IMPs in the studied alloys (AA2024-T3, AA2198-T8, AA2198-T851, and AA7475-T761). Before anodizing, the matrix regions (locations L3, L7, and L12 in Table 2) exhibit a high Al content (>90 wt%), with minor amounts of Cu, Mg, and Zn, depending on the alloy composition.

Regarding the IMPs, distinct compositions were observed across the different alloys. In AA2024-T3, the Al–Cu–Mg and Al–Cu–Fe–Mn–Si phases (locations L1 and L2 in Table 2). In the Al–Cu–Li alloys (AA2198-T8 and AA2198-T851), the identified IMPs (locations L7 and L11 in Table 2) consisted primarily of Al–Cu–Fe phases, which are commonly found in these alloys [39]. In AA7475-T761, two distinct types of IMPs were identified: the first type, observed at location L16 in Table 2, corresponds to Al–Cu–Fe with a relatively high-copper-content (29.8 wt %), while the second type, found at location L15 in Table 2, consists of Al–Cu–Fe with significantly lower-copper-content (5.6 wt%). These findings align with a recent study on the characterization of IMPs, which confirmed that all IMPs in AA2024-T3 and Al–Cu–Li alloys contain high copper levels (>12 wt%), whereas in AA7475-T761, IMPs exhibit either high (>12 wt%) or low (<6 wt%) copper content [40].

After anodizing, oxide flakes were observed at the locations of high-copper-containing IMPs, as indicated by the dashed squares (2, 3, 4, and 5) in Fig. 1 (a2). The anodic film formed on these particles protrudes outward and exhibits cracking, suggesting a porous nature. According to the literature [41], under the same anodizing conditions used in this study, a porous anodic film had not yet developed on the alloy matrix after 5 s of anodizing. Therefore, the distinct features observed in Fig. 1 suggest that high-copper-containing IMPs undergo preferential anodizing compared to the surrounding matrix, which could explain the higher O levels detected over these particles after anodizing (locations L5, L9, L13, and L19 in Table 2).

In contrast, Si-containing IMPs in AA2024-T3 and low-copper-containing IMPs in AA7475-T761 (dashed squares 1 and 6, respectively, in Fig. 1 (a2, d2)) remained intact after anodizing, indicating their low reactivity during the initial stages of the anodizing process. This behaviour is further supported by EDX analysis (locations L4 and L18 in Table 2), where minimal variations in alloying elements and low oxygen concentrations suggest reduced reactivity of these particles in the anodizing environment.

Another noteworthy aspect observed in Fig. 1 (a2–d2) is that not all IMPs underwent anodizing, as this phenomenon appears to be influenced by the size, type, and location of the IMPs within the alloy.

The results in Fig. 1 demonstrate that IMP composition plays a crucial role in their behaviour during anodizing. High-copper-containing IMPs undergo greater elemental depletion, contributing to localized defects in the anodic film. In contrast, Si-containing IMPs in AA2024-T3 and low-copper-containing IMPs in AA7475-T761 exhibit higher stability, potentially reducing dissolution-induced defects. These findings, obtained after 5 s of anodizing, provide insight into the initial interactions between IMPs and the forming anodic film. However, industrial anodizing processes typically involve significantly longer durations [42]. To evaluate the long-term impact of IMP composition under more representative conditions, Fig. 2 presents the behaviour of IMPs after 20 min of anodizing [43].

Fig. 2 presents scanning electron micrographs of the studied aluminum alloys before anodizing (a1–d1) and after anodizing (a2–d2) for 20 min. The dashed squares (1–8) indicate higher-magnification regions, highlighting areas containing IMPs before and after anodizing.

As in Fig. 1, the composition of the matrix before anodizing is reported at locations L4, L11, L17, and L23 in Table 3. In AA2024-T3, three types of IMPs were identified: Al–Cu–Mg, Al–Cu–Fe–Mn, and Al–Cu–Fe–Mn–Si, as indicated at locations L1, L2, and L3 in Table 3. All these phases are high-copper-containing IMPs. Although the Al–Cu–Fe–Mn phase was not specifically mentioned in Fig. 1, its presence in this alloy is confirmed by compositional analysis, consistent with previous studies [41]. In the Al–Cu–Li alloys (AA2198-T8 and AA2198-T851), high-copper-containing IMPs were identified at locations L5, L6, L9, and L10 in Table 3. In contrast, in AA7475-T761, both high-copper-containing IMPs (location L21 in Table 3) and low-copper-containing IMPs (location L22 in Table 3) were identified.

After anodizing, differences were observed between regions with and without IMPs. In the matrix regions (locations L8, L14, L20, and L26 in Table 3), a higher concentration of O and S was detected compared to the values reported in Table 2. This increase is likely attributed to the longer anodizing duration, which promotes further anodic film growth and sulfur incorporation into the film [42].

A common characteristic observed across all studied alloys is the behaviour of high-copper-containing IMPs after anodizing. In Fig. 2 (a2–d2), a reduction in Cu, Fe, Mg, and Mn content, accompanied by an increase in O and S concentrations, was identified (locations L5, L6, L12, L13, L18, L19, and L25 in Table 3), indicating the rapid dissolution of

Table 2
– EDX locations indicated in Fig. 1 (wt%).

Aluminium Alloys	Test condition of surface	Location of EDX points	Elements								
			Al	Cu	Fe	Mg	Mn	O	S	Si	Zn
AA2024-T3	**Before anodizing**	**L1**	61.1	20.1	11.2	–	5.3	–	–	2.3	–
		L2	53.6	30.1	–	16.2	–	–	–	–	–
		L3	94.8	3.7	–	1.5	–	–	–	–	–
	After anodizing	**L4**	79.3	6.1	2.4	–	–	9.7	0.6	1.9	–
		L5	75.5	0.6	–	0.3	–	22.4	1.2	–	–
		L6	79.3	1.1	–	–	–	18.2	1.2	–	–
AA2198-T8	**Before anodizing**	**L7**	57.3	31.2	11.5	–	–	–	–	–	–
		L8	95.8	3.8	–	0.4	–	–	–	–	–
	After anodizing	**L9**	62.4	9.6	5.2	–	–	21.7	1.1	–	–
		L10	81.9	0.6	–	–	–	16.4	1.1	–	–
AA2198-T851	**Before anodizing**	**L11**	48.7	38.6	12.7	–	–	–	–	–	–
		L12	95.8	4.2	–	–	–	–	–	–	–
	After anodizing	**L13**	71.7	3.1	0.5	–	–	23.4	1.3	–	–
		L14	79.7	0.5	–	–	–	19.1	1.2	–	–
AA7475-T761	**Before anodizing**	**L15**	79.2	5.7	15.1	–	–	–	–	–	–
		L16	51.3	29.8	18.9	–	–	–	–	–	–
		L17	90.1	1.8	–	2.1	–	–	–	–	5.9
	After anodizing	**L18**	75.7	5.6	14.9	–	–	3.8	–	–	–
		L19	70.2	2.1	0.5	–	–	25.8	1.4	–	–
		L20	75.9	0.9	–	–	–	20.1	1.2	–	1.9

* Lithium cannot be detected by the EDX employed in the present work. The compositions were determined from representative point analysis of constituent intermetallic particles (IMPs). A comprehensive statistical analysis, including uncertainties and standard deviations based on more than 50 particles per alloy, has been published in our previous work [40].

these particles during anodizing. This phenomenon is associated with element migration dynamics and varying degrees of enrichment at the particle/anodic film interface.

The high-copper-containing IMPs dissolved during anodizing, generating micrometric cavities in the anodic film that retained the original shape of the particles. These features, indicative of the complete dissolution of the IMPs, are clearly visible in Fig. 2 (a1–d1), as indicated by the white arrows within the dashed squares.

Fig. 1 (a2 and d2) shows that some IMPs in AA2024-T3 and AA7475-T761 exhibited notable resistance to dissolution, even after prolonged anodizing. In Fig. 2, Si-containing IMPs (dashed square 3 in Fig. 2 (a1)) and low-copper-containing IMPs (dashed square 8 in Fig. 2 (d2)) remained as residual IMPs after the extended anodizing time. These remnant particles are indicated by the yellow arrows in Fig. 2 (a1 and d1). EDX analysis at locations L7 and L24 in Table 3 confirms the presence of Si in AA2024-T3 and Cu in AA7475-T761, with low O and S concentrations, indicating a significantly slower dissolution rate for these particles.

Given that low-copper-containing IMPs are exclusive to AA7475-T761, their dissolution behaviour requires further investigation. The influence of Cu content on IMP stability during anodizing has been previously explored in the literature [34,41], as copper variation can significantly alter the electrochemical response of these particles. Based on these findings, Fig. 3 provides a more detailed analysis of the anodizing behaviour of AA7475-T761, focusing on the morphological changes in low-copper-containing IMPs after anodizing and anodic film stripping.

The white arrow in Fig. 3 (a) indicates a low-copper-containing IMP, whose chemical composition is confirmed by EDX analysis (locations L1 and L2 in Table 4). Notably, this IMP contains a region of the alloy matrix within its structure, appearing as a darker area inside the IMP, with a contrast similar to that of the surrounding matrix. This contrast difference is attributed to the lower atomic weight of the matrix elements compared to those in the IMP.

During anodizing, an anodic film formed above the IMP, as highlighted by the dashed white arrow in Fig. 3 (b). EDX analysis (locations L3 and L5 in Table 4), corresponding to the anodic film above the IMP and the surrounding matrix, respectively, reveals lower O and S concentrations in the film formed over the IMP compared to the matrix. This observation aligns with the results reported in dashed squares 5 and 8 in Figs. 1 and 2, suggesting that anodic film formation above the IMP occurs at a slower rate, likely due to the lower dissolution kinetics of this specific phase.

Interestingly, the region of matrix contained within the IMP, observed in Fig. 3 (a), appears brighter within the anodic film above the IMP after anodizing. EDX analysis (location L4 in Table 4) confirms the presence of Cu and Fe in this region, with low concentrations of O, suggesting that this portion of the IMP was initially embedded below the surface of the matrix. During anodizing, as the IMP dissolved and the matrix above it was consumed, the previously contained region of the IMP became exposed. Since this area was not in direct contact with the electrolyte during the early stages of anodizing, its dissolution was slower, leading to its retention above the anodic film.

To further investigate this feature, the anodic film above the IMP was removed by immersion in ultrapure distilled water under ultrasonic agitation, as shown in Fig. 3 (c). After the removal of the anodic film, the IMP becomes clearly visible beneath it, as highlighted by the white dotted arrow in Fig. 3 (c). Due to its higher atomic weight compared to the surrounding anodic film, it appears brighter in the BSE image. EDX analysis (location L6 in Table 4) confirms the chemical composition of this low-copper-containing IMP, whereas EDX analysis (location L7 in Table 4), corresponding to the surrounding matrix, reveals an increase in oxygen levels, likely due to anodic film hydration during the ultrasonic treatment. The lack of film removal in the adjacent matrix region suggests that the anodic film formed above the IMP exhibited lower adhesion compared to the film formed on the IMP-free matrix region, indicating differences in film properties depending on the underlying phase composition.

Given that high-copper-containing IMPs are present in all studied alloys and exhibit distinct dissolution behaviour during anodizing, a more detailed analysis of these particles was conducted. Fig. 4 provides a comprehensive evaluation of the morphological and compositional changes in these phases.

Fig. 4 (a1–d1) displays the surfaces of the aluminum alloys before anodizing, while Fig. 4 (a2–d2) shows the same areas after anodizing. The dashed squares highlight specific regions of interest, focusing on IMPs before anodizing (1, 3, 5, and 7) and after anodizing (2, 4, 6, and 8).

As observed on the alloy surfaces prior to anodizing (Fig. 4 (a1–d1)), IMPs were present across all alloys. After the anodizing process (Fig. 4

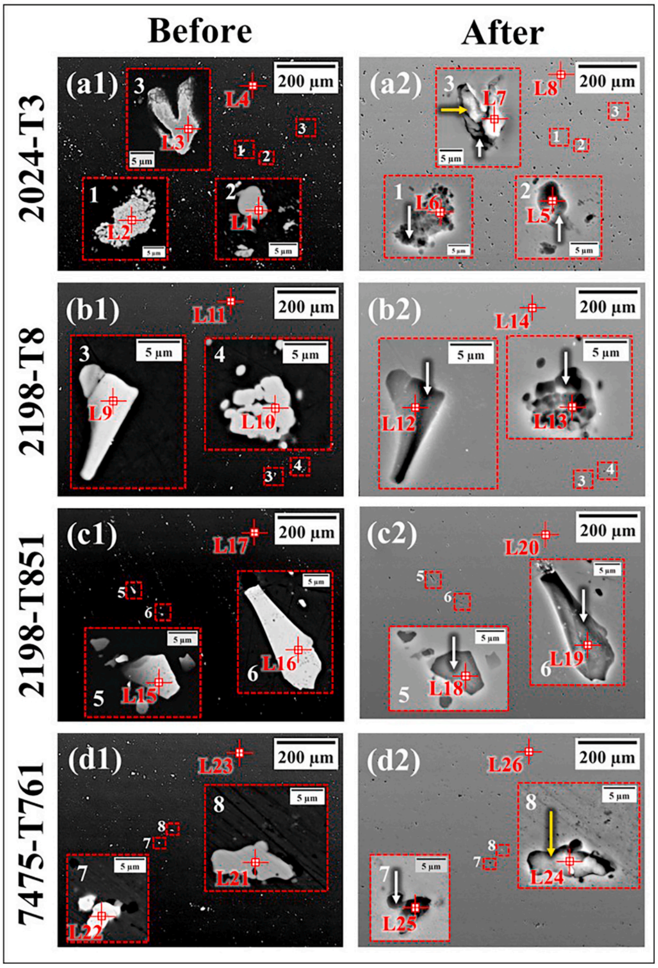

Fig. 2. – Scanning electron micrographs of aluminium alloys at lower magnification, before (a1–d1) and after (a2–d2) anodizing for 20 min. The red dashed squares (1–8) indicate higher magnification regions containing constituent intermetallic particles (IMPs) before and after anodizing. All images were acquired in backscattered electron (BSE) mode at an accelerating voltage of 20 kV. (For interpretation of the references to colour in this figure legend, the reader is referred to the Web version of this article.)

(a2–d2)), the dissolution of these particles led to the formation of cavities in the anodic film of all studied alloys. The population densities of these surface cavities in AA2024-T3, AA2198-T8, AA2198-T851, and AA7475-T761 followed the order: 3.9×10^3, 2.7×10^3, 2.1×10^3, and 7.2×10^2 per cm^2, respectively. This trend is consistent with the IMP distribution previously reported in the literature [40], which demonstrated that AA2024-T3 contains the highest number of high-copper-containing IMPs, followed by the AA2198 alloys and finally AA7475-T761. Consequently, alloys with a higher number of high-copper-containing IMPs exhibit a higher number of cavities in the anodic film after anodizing.

The dashed squares in both sets of images highlight areas that, at higher magnification, reveal the dissolution of IMPs, as confirmed by the EDX maps (Fig. 4(e and f)). These maps show high Cu and Fe concentrations in the IMPs before anodizing, whereas after the process, a significant increase in O and Al is observed, indicating the formation of the anodic film. This behaviour can be explained by the faster migration rates of Fe, Mn, and Cu compared to Al [11]. The selected regions, highlighted by the dashed squares before (Fig. 4 (a1–d1)) and after (Fig. 4 (a2–d2)) anodizing, were further analyzed to investigate the morphology of the dissolved IMP sites.

Fig. 5 provides a detailed examination of the cavities formed by the dissolution of high-copper-containing IMPs, offering a comprehensive understanding of their morphological features and surface topography. To enhance the visualization of these regions, dashed squares 2, 4, 6, and 8 were analyzed in secondary electron (SE) mode at a reduced accelerating voltage.

In Fig. 5 (a1–d1), the bright areas observed in the cavity regions result from electron beam charging, caused by discontinuities in the anodic film due to the dissolution of IMPs. When the accelerating voltage is reduced to 1.5 kV, the cavities formed by the dissolved IMPs become more distinct (Fig. 5 (a2–d2)). At higher magnifications, as highlighted by the red dashed squares (1–8) in Fig. 5 (a3–d4), morphological variations associated with the shape of the dissolved IMPs during anodizing are evident. These variations lead to protrusions on the anodic film surface.

Table 5 presents the average depth of these cavities, measured by AFM for 20 cavities in each alloy.

The cavity depth values correspond to the size of the IMPs within the alloy matrix, indicating that relatively large intermetallic particles can expose the underlying alloy or reduce the thickness of the anodic film. This observation is further supported by the standard deviation values, which reveal that the cavity depths are comparable to or exceed the thickness of the anodic film.

A more detailed surface analysis of an aluminium alloy before and after anodizing, using AFM, is provided in Fig. 6. The results specifically focus on the AA7475-T761 alloy, where the dissolution of IMPs, particularly those with high-copper-containing, leads to the formation of surface cavities. Due to the consistent nature of this behaviour across different materials with high-copper-containing IMPs (Figs. 2 and 4), data for the other samples has not been presented in detail.

Fig. 6 (a) presents surface topography maps before and after anodizing, focusing on a region containing IMPs and the cavities formed by their dissolution. The topographic profiles, represented by the red dashed lines below the maps, provide an analysis of the height of the IMPs and the depth of the resulting cavities. The protrusions within the cavities become more evident when the oxide surface is tilted, as shown in Fig. 6 (b), where the region highlighted in Fig. 6 (a) is displayed at higher magnification (Fig. 6 (b 1)). The discontinuity in the oxide film, observed in the topographic spectrum of Fig. 6 (a), becomes more pronounced at higher magnification (Fig. 6 (b 2)), clearly revealing the discontinuities in the area associated with the dissolution of the IMP.

Additionally, a cross-sectional analysis of a region containing a cavity was conducted, as illustrated in Fig. 6 (c). Fig. 6 (c1) provides a low-magnification view of the region with a defect in the oxide surface. At higher magnifications in the area associated with the defect (Fig. 6 (c3, c4)), the discontinuities and protrusions related to the cavity are evident, with a depth of ~1.1 μm, approximately one-third of the anodic film thickness.

Considering the results presented in Fig. 6, which suggest that the initial position of the IMPs influences the formation and characteristics of cavities in the anodic films, further cross-sectional analysis is necessary to better understand their spatial distribution and impact on the overall film integrity. This aspect is explored in the following section.

3.2. *Anodizing behaviour of constituent intermetallic particles (IMPs): Cross-sectional analysis*

Fig. 7 presents a cross-sectional analysis of the anodic films, providing further insight into the spatial distribution of cavities formed by the dissolution of IMPs and their impact on film integrity.

Fig. 7 (a) shows the cross-section of the anodic film formed on the AA2198-T8 alloy, with an approximate thickness of 2.8 μm in a defect-free region. Higher magnification images of regions A-C, shown in Fig. 7 (a1-a3), reveal cavities (1–3) associated with the dissolution of high-copper-containing IMPs. The distances of these defects from the alloy substrate vary based on the initial position of the IMPs. In Fig. 7 (a1), defect (1) is ~1.1 μm from the film surface and ~1.3 μm from the

Table 3
– EDX locations indicated in Fig. 2 (wt.%).

Aluminium Alloys	Test condition of surface	Location of EDX points	Elements								
			Al	Cu	Fe	Mg	Mn	O	S	Si	Zn
AA2024-T3	**Before anodizing**	**L1**	62.7	25.7	–	11.6	–	–	–	–	–
		L2	73.2	17.3	5.1	–	4.4	–	–	–	-
		L3	75.3	11.2	5.7	–	4.6	–	–	3.2	-
		L4	95.5	3.4	–	1.1	–	–	–	–	–
	After anodizing	**L5**	65.1	1.1	–	–	–	32.6	1.2	–	–
		L6	63.3	0.9	–	–	–	34.7	1.1	–	–
		L7	74.8	0.8	–	–	–	20.8	1.1	2.5	–
		L8	63.1	–	–	–	–	35.7	1.2	–	–
AA2198-T8	**Before anodizing**	**L9**	57.4	30.2	12.4	–	–	–	–	–	–
		L10	59.5	28.7	11.8	–	–	–	–	–	–
		L11	96.4	3.2	–	0.4	–	–	–	–	–
	After anodizing	**L12**	65.1	0.9	–	–	–	32.8	1.2	–	–
		L13	64.8	0.7	–	–	–	33.4	1.1	–	–
		L14	62.1	–	–	–	–	36.7	1.2	–	–
AA2198-T851	**Before anodizing**	**L15**	51.2	35.4	13.4	–	–	–	–	–	–
		L16	54.7	30.8	14.5	–	–	–	–	–	–
		L17	96.1	3.4	–	0.5	–	–	–	–	–
	After anodizing	**L18**	65.1	0.6	–	–	–	33.1	1.2	–	–
		L19	68.2	0.9	–	–	–	29.7	1.2	–	–
		L20	63.5	–	–	–	–	35.9	1.3	–	–
AA7475-T761	**Before anodizing**	**L21**	77.1	5.8	17.1	–	–	–	–	–	–
		L22	53.3	30.2	16.5	–	–	–	–	–	–
		L23	90.1	1.1	–	2.6	–	–	–	–	6.2
	After anodizing	**L24**	69.3	4.2	3.1	–	–	22.8	0.6	–	–
		L25	68.2	0.4	–	–	–	30.1	1.3	–	–
		L26	62.5	–	–	–	–	35.2	1.2	–	1.1

* Lithium cannot be detected by the EDX employed in the present work. The compositions were determined from representative point analysis of constituent intermetallic particles (IMPs). A comprehensive statistical analysis, including uncertainties and standard deviations based on more than 50 particles per alloy, has been published in our previous work [40].

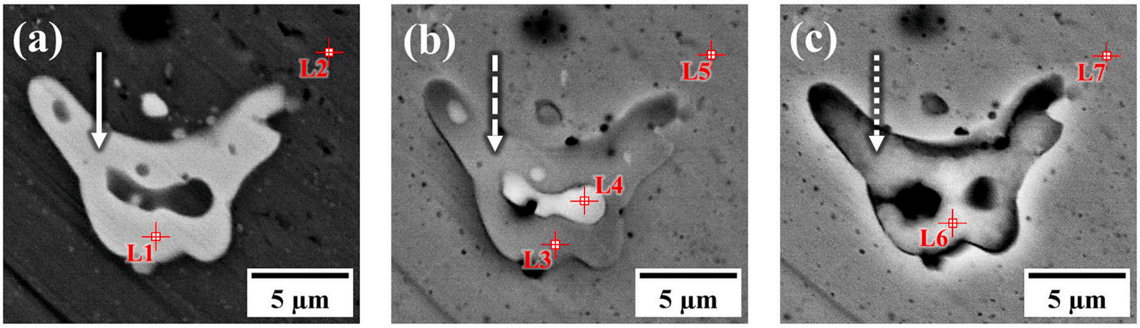

Fig. 3. – Scanning electron micrographs of the AA7475-T761 anodized aluminium alloy for 20 min: (a) before anodizing; (b) after anodizing; (c) after oxide removal over a low-copper-containing constituent intermetallic particle (IMP). The white arrow indicates low-copper-containing IMP, while the dashed white arrow highlights the anodic film formed above the IMPs after anodizing. In (c), the dotted white arrow points to a residual IMP within the anodic film. All images were acquired in backscattered electron (BSE) mode at an accelerating voltage of 20 kV.

substrate, suggesting an IMP initially located below the alloy surface, resulting in a mid-film defect. In Fig. 7 (a2), a distance of ~2.2 μm from defect (2) to the substrate suggests an IMP originally at the alloy surface, producing a defect near the anodic film surface. Defect (3) in Fig. 7 (a3) is ~1.7 μm from the substrate, indicating an IMP closer to the surface that became occluded within the film during anodizing. These observations indicate that the initial position of IMPs in the aluminium matrix influences the final location of defects in the anodic film. Additionally, the original defect sizes, ranging from 0.5 to 1 μm, suggest that smaller IMPs may lead to less significant discontinuities in the film.

In contrast, Fig. 7(b–e) shows cross-sections of anodic films for various aluminium alloys, where defect depths and sizes often exceed the film thickness. In Fig. 7 (b), the AA2024-T3 alloy shows a cavity of 9.1 μm in size and 2.9 μm in depth, exceeding the 2.3 μm film thickness. Similarly, Fig. 7 (c) shows the AA2198-T8 alloy with a cavity of 10.2 μm and a depth of 2.8 μm, exceeding the defect-free film thickness of 2.7 μm. In Fig. 7 (d), the AA2198-T851 alloy has a cavity of 6.1 μm with a depth of 2.8 μm, larger than the 2.6 μm film thickness. Finally, Fig. 7 (e) shows the AA7475-T761 alloy, where a cavity of 11.1 μm and a depth of 3.9 μm is very close to the 4.1 μm film thickness, indicating that the dissolution of larger IMPs significantly compromises the structural integrity of the anodic film.

The results reported in Figs. 6 and 7 agree with the hypothesis in the literature that the size and distribution of IMPs within the aluminium matrix significantly influence the integrity of the anodic film [27,44]. Larger and more strategically positioned IMPs can lead to the formation of deeper cavities (Fig. 7(d–e)), which compromise the structural integrity of the anodic film and impact the overall performance of the aluminium alloy.

According to the field-assisted dissolution (FAD) theory, IMPs play a crucial role in modifying anodic films by altering the local electric fields at the surface during anodizing. This directly impacts anodic film formation, causing distortions in film growth [27,45–47], which leads to irregularities in the film morphology and compromises its integrity,

Table 4
– EDX locations indicated in Fig. 3 (wt.%).

Condition	Location of EDX points	Al	Cu	Fe	Mg	Zn	O	S
Before anodizing	**L1**	75.2	5.7	19.1	–	–	–	–
	L2	89.7	1.7	–	2.4	6.2	–	–
After anodizing	**L3**	83.5	0.6	–	–	–	15.1	0.8
	L4	–	4.8	1.2	–	–	6.3	–
	L5	67.7	–	–	–	0.9	30.2	1.2
After the film stripping above the IMP	**L6**	74.9	5.4	7.8	–	–	11.2	0.7
	L7	55.8	–	–	–	0.8	42.3	1.1

particularly at the film/alloy interface. These effects are even more pronounced in high-resolution ultramicrotomed images, as shown in Fig. 8.

Fig. 8 (a, b) shows scanning electron micrographs obtained in BSE and SE modes of a region within the anodic film containing a cavity formed by the dissolution of a high-copper-containing IMP. The dashed white circle in Fig. 8 (a) indicates the location of the cavity, which formed near the film surface.

In Fig. 8 (b), arrow ’a’ represents the thickness of the anodic film in a defect-free region, measuring approximately 2.3 μm. The continuity of the anodic film is marked by the dashed line ’A’, which separates the thickness of the film below the cavity, indicated by arrow ’b’ (~1.6 μm), from the thickness at the film/alloy interface, indicated by arrow ’c’ (~0.6 μm). This region is characterized by a discontinuity in the anodic film located below the cavity at the film/alloy interface. The dashed line ’B’ represents the interface between the cavity and the onset of the anodic film beneath it. The size of the cavity is approximately 0.5 μm, as indicated by arrow ’d’. The combined distances of ’a’ and ’c’ total ~2.1 μm, which is close to the overall film thickness.

This result (Fig. 8) suggests that the rapid dissolution of the IMP during the early stages of anodizing allows the anodic film to continue growing around the cavity, thereby promoting film formation directly beneath the dissolved IMP, resulting in discontinuity in the anodic film, as indicated by arrow ’c’.

At higher magnification of the region associated with cavity formation (Fig. 8 (c)), a significant change in the growth direction of the anodic film within the recessed areas of the cavity can be observed, as highlighted by the red dashed lines. This change in orientation — from perpendicular to the material surface to perpendicular to the cavity surface — clearly demonstrates the direct impact of IMP dissolution on the final structure of the anodic film. These morphological changes provide compelling evidence of the influence of IMPs on film growth, leading to discontinuities in pore growth direction and the formation of spherical features beneath the cavities, as observed in Figs. 6 and 7. Some authors have reported [27,45,46,48,49] that such discontinuities

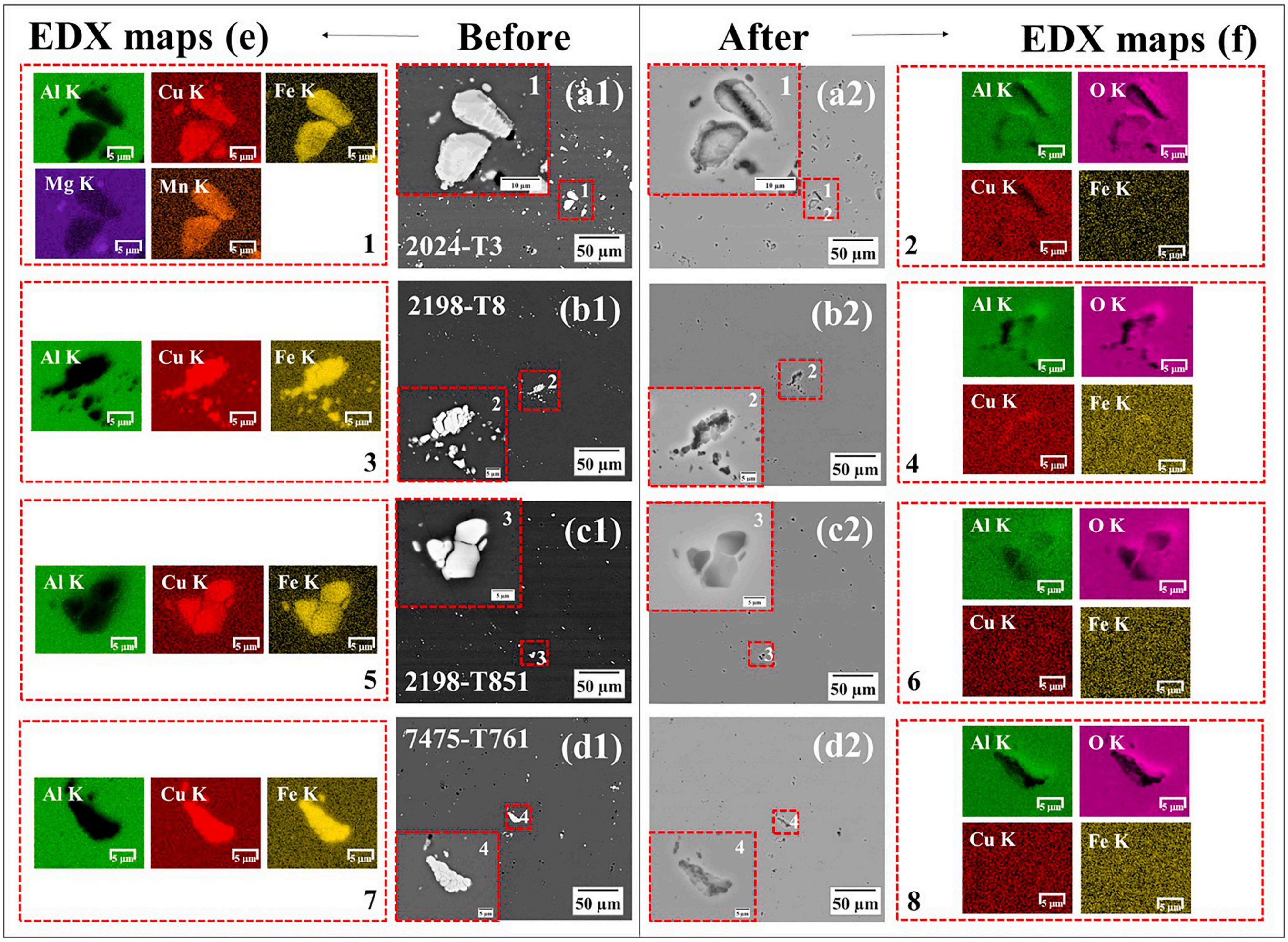

Fig. 4. – Scanning electron micrographs of the anodized aluminium alloys for 20 min: (a1–d1) lower magnification images showing constituent intermetallic particles (IMPs) before anodizing; (a2–d2) IMPs after anodizing. The red dashed squares in all images (1–4) highlight regions containing only high-copper-containing IMPs at higher magnification. Figures (e) and (f) present EDX maps of these regions before and after anodizing. (For interpretation of the references to colour in this figure legend, the reader is referred to the Web version of this article.)

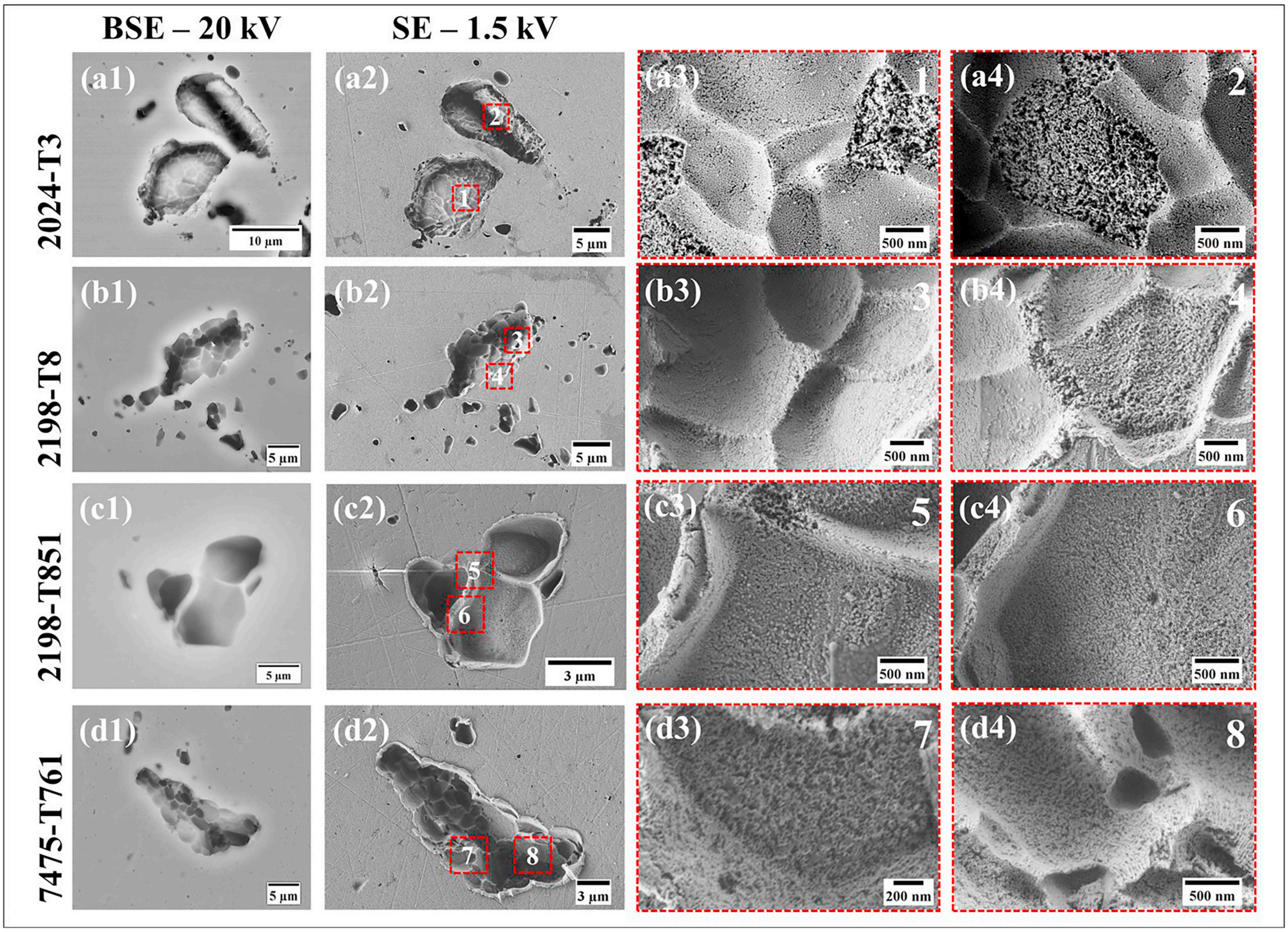

Fig. 5. – Scanning electron micrographs of the anodized aluminium alloys showing regions where high-copper-containing constituent intermetallic particles (IMPs) dissolved during the anodizing process: (a1–d1) images obtained at an accelerating voltage of 20 kV; (a2–d2) images obtained at an accelerating voltage of 1.5 kV; and (a3–d3) higher magnification of the dashed squares in (a2–d2). The images in (a1–d1) were obtained in BSE mode, while those in (a2–d4) in secondary electron (SE) mode at an accelerating voltage of 1.5 kV, respectively.

Table 5

– Average size of cavities on the surface of Al alloys caused by the dissolution of high-copper-containing constituent intermetallic particles (IMPs) during anodizing in TSA solution for 20 min.

Al – alloys	Average depth of the cavities (µm)
AA2024-T3	1.5 ± 0.8
AA2198-T8	1.7 ± 0.9
AA2198-T851	1.5 ± 1.1
AA7475-T761	2.4 ± 1.4

* Values calculated using the AFM technique in tapping mode.

in the anodic film contribute to reduced corrosion resistance in anodized aluminium alloys.

These findings indicate that upon dissolution, a high-copper-containing IMP creates a void (cavities) within the anodic film comparable in size to the original intermetallic particle. The dissolution process of the IMP can lead to the formation of various types of cavities, depending on the initial position of the IMP within the alloy matrix. These observations are further illustrated in Fig. 9.

Fig. 9 shows regions of the anodic film where cavities have either formed or are absent. The anodic film is uniform in areas without cavities (Fig. 9(a–d)). However, the initial position of the IMPs within the alloy matrix leads to the formation of distinct types of cavities in the anodic film. These cavities, indicated by red arrows, are observed at different locations: at the surface (Fig. 9 (a1-d1)), within the film (Fig. 9 (a2-d2)), near the surface (Fig. 9(a3-d3)), and at the interface between the film and the alloy (Fig. 9 (a4-d4)). The cavity size correlates with the size of the IMPs in the alloys (Figs. 1 and 2), and their morphology is shaped by the dissolution of the IMPs.

The results presented up to this point, particularly the observations in Figs. 6–9, pertain to the dissolution of high-copper-containing IMPs, which dissolve more rapidly than the alloy matrix. However, as illustrated in Fig. 2, for the AA2024-T3 and AA7475-T761 alloys, IMPs containing silicon (dashed square 3 in Fig. 2 (a1)) and those with low-copper-containing (dashed square 8 Fig. 2 (d1)) exhibited a slower dissolution rate during anodizing when compared to the alloy matrix. Fig. 10 further explores how these differences in dissolution rates of Si-containing and low-copper-containing IMPs affect the structure of the anodic film, highlighting the formation of a distinct morphology resulting from the slower dissolution of these particles.

Fig. 10(a) and (b) present scanning electron micrographs of ultramicrotomed cross-sections of AA2024-T3 and AA7475-T761, respectively. These alloys exhibited IMPs positioned at the film/alloy interface, with distinct chemical compositions that play a crucial role in influencing the formation of the anodic film. In Fig. 10 (a1), the IMP in the AA2024-T3 alloy contains 65.1 wt% Al, 15.5 wt% Cu, 11.1 wt% Fe, 5.2 wt% Mn, and 3.1 wt% Si, indicative of an Al–Cu–Fe–Mn–Si particle. By contrast, Fig. 10(b1) shows a particle in the AA7475-T761 alloy containing 78.5 wt% Al, 5.4 wt% Cu, and 16.1 wt% Fe, characteristic of a

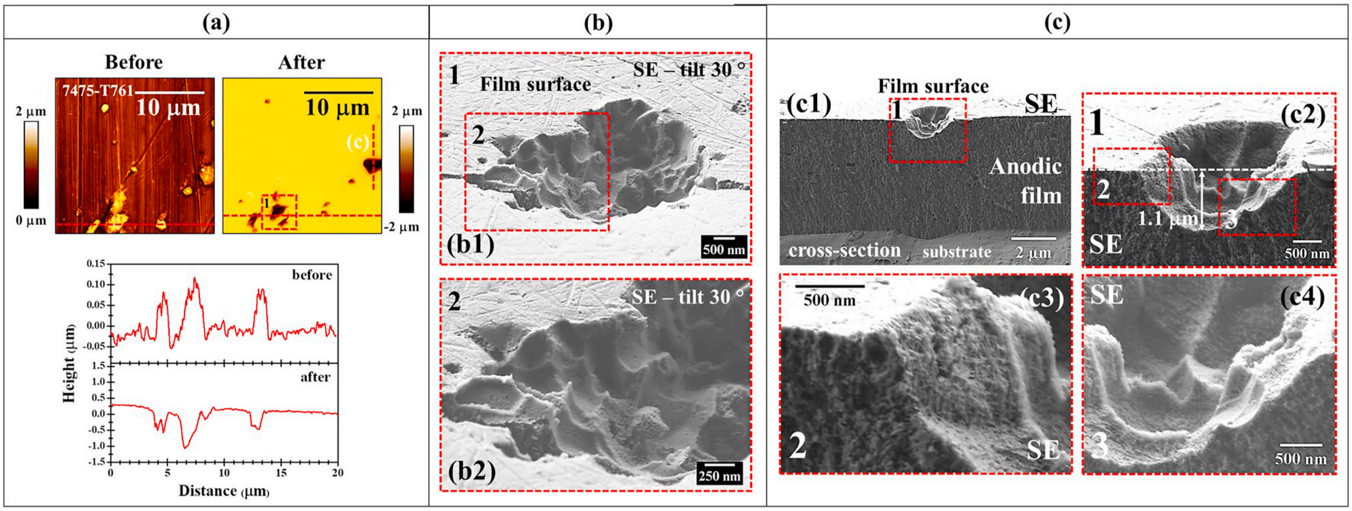

Fig. 6. – (a) AFM surface topography of the AA7475-T761 alloy surface before and after anodizing, showing a region with constituent intermetallic particles (IMPs). Below the maps are topography line profiles (red dashed lines) across the intermetallic particles indicated in the maps, before and after anodizing; (b) scanning electron micrograph of the dashed square in (a) after anodizing, at (b1) lower magnification and (b2) higher magnification; (c) cross-section along the dashed line in (a), showing the defect caused by the dissolution of the IMP, with images (c1–c4) at increasing magnifications. The cross-sections presented in (c) were prepared by mechanical bending. Images in (b) and (c) were obtained in secondary electron (SE) mode at an accelerating voltage of 1.5 kV, respectively. (For interpretation of the references to colour in this figure legend, the reader is referred to the Web version of this article.)

low-copper-contend particle.

The IMPs in Fig. 10 (a1, a2) and (b1, b2) protrude into the anodic film, indicating that they dissolve more slowly than the surrounding alloy matrix. The ratio a/b, which represents the distance from the dashed line (A) to the film/alloy matrix interface compared to the distance from the line (B) to the film/particle interface, was calculated as 0.53 in Fig. 10 (a1) and 0.45 in Fig. 10 (b1). These values suggest that the particles anodize at approximately half the rate of the matrix, leading to the slower growth of the anodic film over the particles compared to the surrounding alloy.

Additionally, the film morphology at the film/IMP interface (Fig. 10 (a3, a4) and (b3, b4)) exhibits higher porosity than the film/alloy interface. In Fig. 3, the oxide formed above the IMPs was observed; however, it was not possible to resolve the cross-sectional morphology of the film at the IMP interface. The findings in Fig. 10 suggest that the incomplete dissolution of IMPs contributes to the formation of porous regions within the anodic film, which may affect its structural integrity.

These findings demonstrate that variations in the chemical composition of IMPs, such as the presence of Si-containing or low-copper-containing IMPs, can significantly influence the anodizing rate and the subsequent growth of the anodic film. Similar behaviour has been reported for low-copper-containing IMPs in AA2099 Al–Cu–Li alloy [41], showing consistency with the results observed in AA7475-T761 in this study (Fig. 10 (b)) Additionally, previous studies [1] have suggested that Si-containing IMPs may dissolve at a slower rate than the matrix, leading to irregularities in the oxide, a hypothesis supported by our results (Fig. 11 (a)).

Importantly, both the complete and partial dissolution of IMPs can adversely affect the integrity of the anodic film. Therefore, understanding the dissolution rates of different IMPs during anodizing is crucial for optimizing film performance.

4. Discussion

The results reported in Figs. 1 and 2 demonstrate that the anodizing behaviour of IMPs in the alloys cannot be generalized, as small variations in their chemical composition significantly influence their dissolution rates. This selective dissolution contributes to localized defects at the surface, within the anodic film, and at the film/alloy interface. These defects result from either the complete (Fig. 9) or partial (Fig. 10) dissolution of the IMPs, as further illustrated in Fig. 11.

Fig. 11 illustrates the behaviour of IMPs during anodizing and their influence on the formation of defects. The initial surface condition (stage 1) represents the air-formed oxide film on the aluminum matrix and the location of IMPs in a cross-sectional view. The positioning of these particles determines their interaction with the electrolyte during anodizing, directly influencing the formation and spatial distribution of defects in the anodic film. As anodizing progresses (stages 2–4), different defect mechanisms arise depending on the fate of the IMPs: complete dissolution (Fig. 11(a and b and c)), retention within the anodic film (Fig. 11 (d)), or partial dissolution (Fig. 11 (e)). The final morphology and location of these defects are presented in stage 5.

Fig. 11(a–c) illustrates the anodizing behaviour of high-copper-containing IMPs (>12 wt%), located either at the alloy surface or embedded within the matrix. At the onset of anodizing (stage 2), high-field ionic conduction drives the outward migration of Al^{3+} ions from the matrix, while O^{2-} ions migrate inward, leading to anodic film growth at both the metal/film and film/electrolyte interface [50]. In acidic media, Al^{3+} ions reaching the oxide/electrolyte interface are ejected into the electrolyte, contributing to aluminum dissolution and facilitating porous film growth [51,52]. Approximately 40 % of the anodic film thickness develops at the film/electrolyte interface, while the remaining 60 % forms at the metal/film interface a growth ratio that remains consistent across anodizing conditions due to cooperative ionic transport [47].

However, IMPs, particularly those rich in copper, dissolve preferentially during anodizing. The presence of Mg, Fe, and Mn in these particles further enhances anodic dissolution in the acidic electrolyte [4,53]. The high electrical conductivity of Cu-rich IMPs also creates preferential pathways for the electric current compared to the surrounding matrix where anodic film (with a barrier layer) is being formed, accelerating particle dissolution [1,54]. As anodizing progresses (stage 3), defect formation becomes more pronounced, with cavity enlargement accompanying film growth on alloy matrix. Depending on the initial location of the IMP in the matrix, different types of defects can be observed during anodizing as the particle dissolves. These defects may appear on the surface, within the anodic film, or at the film/alloy interface, as illustrated in Fig. 11(a–c) and reported Fig. 9.

The electric field distribution around these IMPs (stage 4) influences pore orientation within the anodic film (Fig. 8). This distortion results

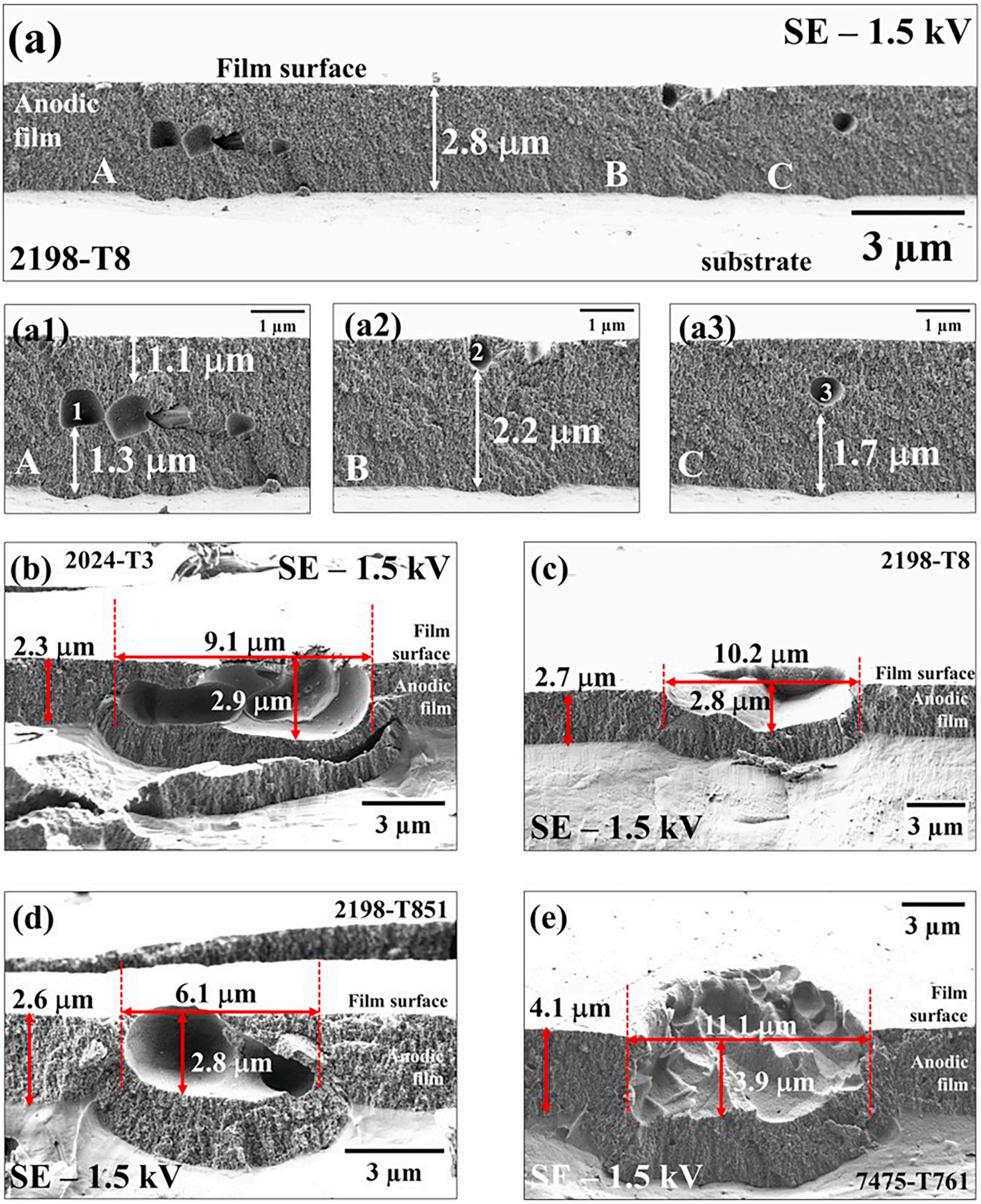

Fig. 7. – Scanning electron micrographs of mechanically bent cross-sections of anodized aluminium alloys for 20 min: (a) lower magnification of the cross-section of the anodic film formed on the AA2198-T8 alloy; (a1–a3) higher magnification of regions A–C in (a); (b–e) cross-sections of anodic films highlighting defects that exceed the film thickness. All images were acquired in secondary electron (SE) mode at an accelerating voltage of 1.5 kV.

from localized alterations in the electric field, induced by the rapid dissolution of the particles, ultimately leading to deviations in pore alignment [55]. In the final stage (stage 5), the complete dissolution of the IMPs gives rise to voids in the region they previously occupied, while the anodic film continues to grow beneath them. This process results in hemispherical features forming beneath the former particles, generating characteristic defects and discontinuities at the film/alloy interface (Fig. 8).

Fig. 11 (d) illustrates the anodizing behaviour of Si-rich IMPs (>10 wt% Si), which were not observed in this study but have been extensively reported in literature, particularly in AA2024 alloys [1,56]. These particles remain intact in acidic anodizing baths due to their low reactivity and high electrical resistance, while the electric current concentrates in the surrounding matrix, leading to selective aluminum oxidation and occluded the particles within the anodic film (stages 2–4).

Fig. 11 (e) depicts the anodizing behaviour of low-copper-containing IMPs, particularly in AA7475-T761 (6 wt% Cu IMPs) and AA2024-T3 (Fe–Mn–Si IMPs as shown in Fig. 10). At the initial stage (stage 2), the surrounding aluminum matrix oxidizes more rapidly, while Fe–Mn –Si and low-copper-containing IMPs exhibit slower oxidation kinetics, resisting current flow. These particles also form a porous anodic film although not protective due to the absence of a barrier layer. Si, Fe, Mn,

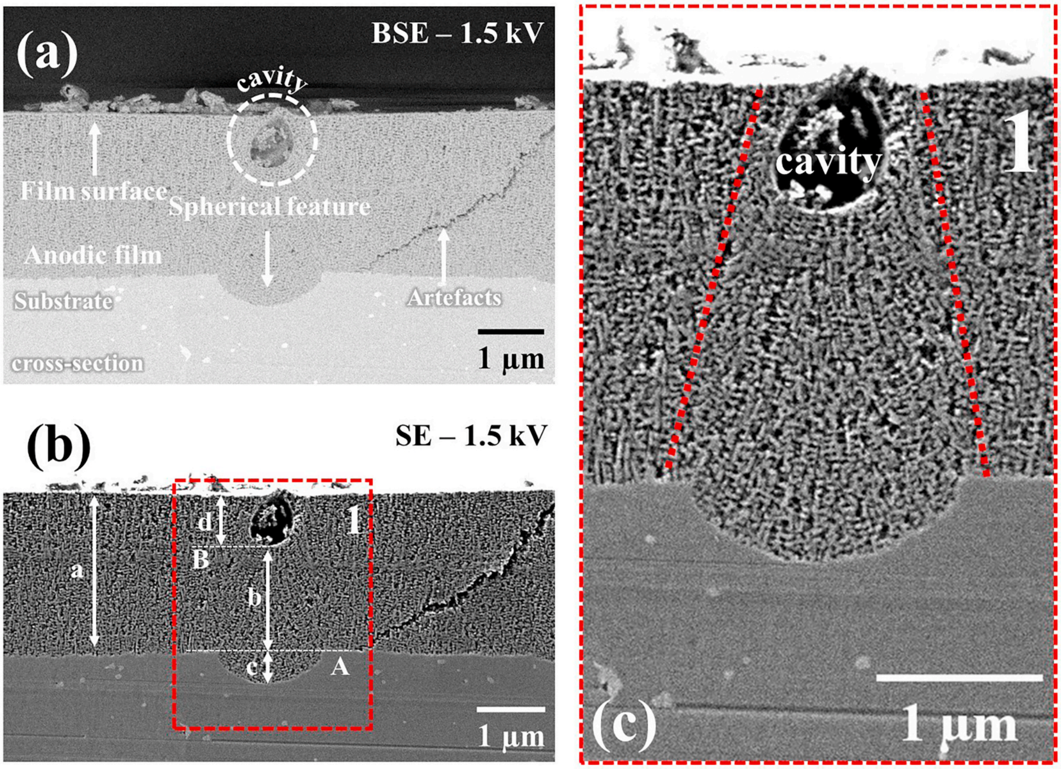

Fig. 8. – Scanning electron micrographs of ultramicrotomed cross-sections of the AA2024-T3 alloy after anodizing for 20 min: (a) cross-sectional image obtained with backscattered electrons (BSE); (b) cross-sectional image obtained with secondary electrons (SE); and (c) higher magnification of the dashed region in (b). The white dashed circle in (a) indicates a cavity formed near the film surface due to the dissolution of a high-copper-containing constituent intermetallic particle (IMPs). All images were acquired at an accelerating voltage of 1.5 kV.

and Cu enrich at the particle/oxide interface, hindering further dissolution [29,57].

In AA2024, Fe, Mn, Si-containing IMPs with high-copper-content (~15 wt% Cu) exhibit behaviour similar to low-copper-containing IMPs, as the enrichment of Fe, Mn and Si delays the dissolution of other elements within the particle, reducing the overall oxidation rate [29,58]. As a result, the matrix surrounding these particles recedes more rapidly, leading to protrusion of the IMPs into the anodic film (Fig. 10). This behaviour is quantified by the a/b ratio, which remains <1, indicating that these particles anodize at approximately half the rate of the matrix (Fig. 10 (a1, b1)). Because of the higher Gibbs free energy required to form Cu, Si, Fe and Mn oxides, these elements accumulate at the film/particle interface, resulting in a highly porous anodic film caused by O_2 evolution (Fig. 10 (a3, b3)) over these IMPs (stage 4).

The results indicate that low-copper-containing IMPs are oxidized more slowly, forming a stable, though porous, anodic film. In contrast, high-copper-containing IMPs dissolve rapidly, resulting in cavities in the resultant anodic films due to the high solubility of Cu oxides in the electrolyte.

A thorough understanding of how IMPs affect anodic film properties can help with the development of predictive models to optimize anodizing conditions and reduce critical defects, thereby improving the performance of anodic films [16]. Advanced characterization techniques, such as X-ray tomography and 3D volumetric reconstruction, can improve defect analysis and provide more accurate predictive models [59,60]. Additionally, machine learning and computational simulations could be employed to predict defect formation and optimize anodizing parameters in real-time [61]. Such approaches would enable automated optimization of alloy compositions and anodizing conditions, facilitating the development of high-performance aluminum alloys with improved mechanical strength and corrosion resistance.

5. Conclusions

Based on the present investigation, respective conclusions can be highlighted regarding the role of constituent intermetallic particles (IMPs) in defect formation during anodizing:

a) The chemical composition of IMPs plays a critical role in the formation of defects in anodic films during anodizing. The preferential dissolution of specific IMPs directly influences the morphology and continuity of resultant anodic films, ultimately affecting their structural integrity.
b) High-copper-containing IMPs (>12 wt% Cu) are strongly associated with the formation of cavities and discontinuity in anodic films, significantly degrading their structural integrity. Their rapid dissolution during anodizing generates micrometer-sized cavities in anodic films. The size of the defects is proportional to the initial size of the particles.
c) In the AA2024-T3, Fe, Mn, Si (Cu) particles, and in the AA7475-T761, low-copper-containing IMPs (<7 wt% Cu), exhibit a lower oxidation rate compared to the surrounding alloy matrix. These IMPs are partially oxidized and partially maintained within the anodic film. The lower oxidation rate of some particles often results in local protrusion of alloy substrate into anodic film, affecting film thickness uniformity. Their incomplete oxidation also leads to local compositional heterogeneity of the resultant anodic films.
d) The differences in anodizing behaviour among IMPs confirm that small variations in chemical composition might significantly influence their oxidation kinetics. This highlights the importance of tailoring anodizing parameters to minimize defect formation, particularly in alloys with a high population density of reactive IMPs.

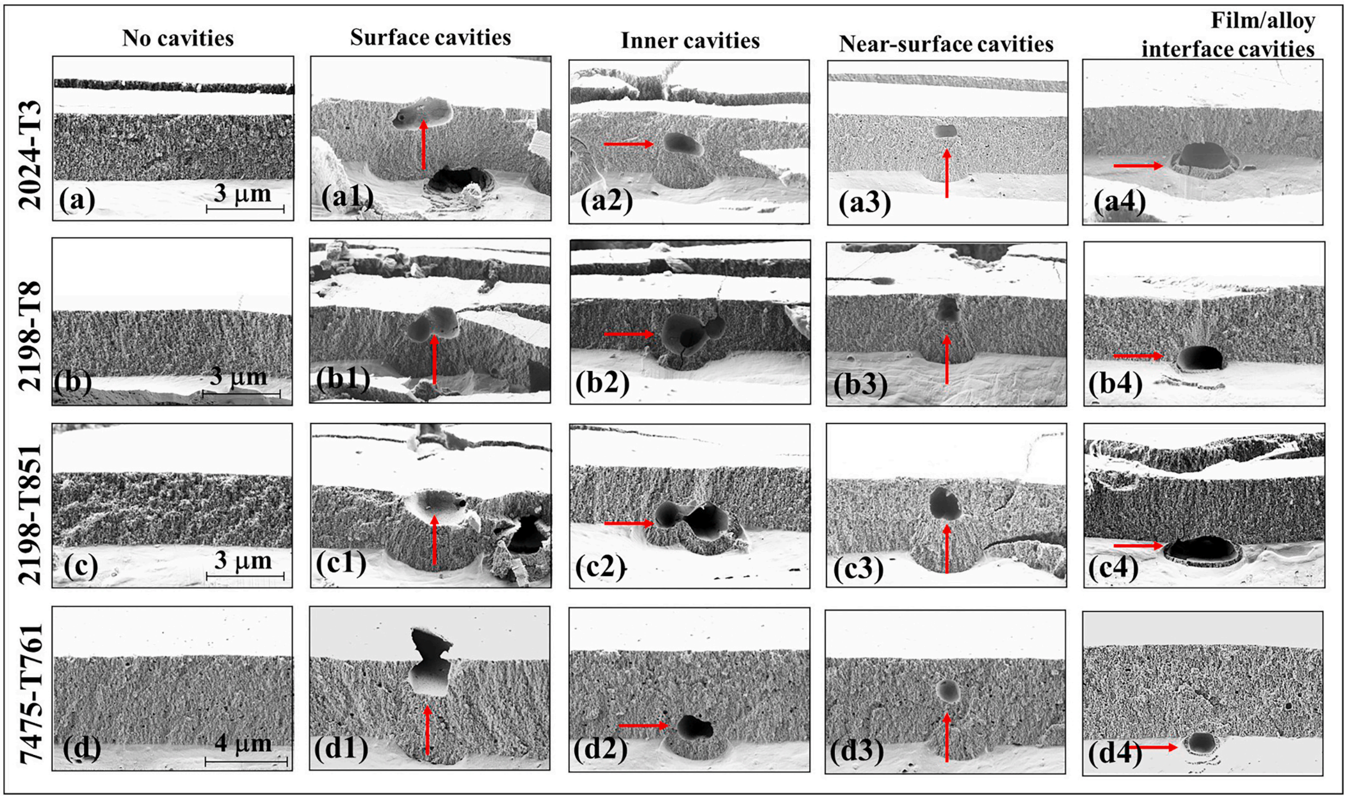

Fig. 9. – Scanning electron micrographs of cross-sections of anodized aluminium alloys for 20 min: anodic films with no cavities (a–d); cavities at the surface (a1–d1); cavities within the film (a2–d2); cavities near the oxide surface (a3–d3); and cavities at the film/alloy interface (a4–d4). All images were acquired in secondary electron (SE) mode at an accelerating voltage of 1.5 kV. Cross-sections were prepared by mechanical bending.

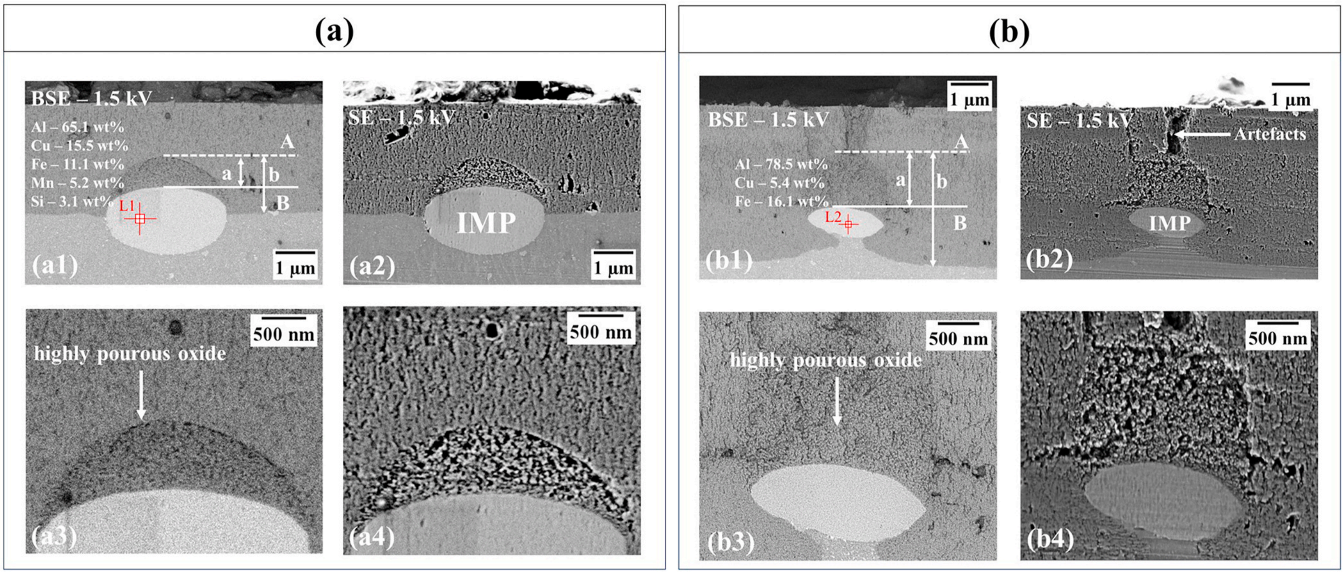

Fig. 10. – Scanning electron micrographs of ultramicrotomed cross-sections after anodizing for 20 min: (a) AA2024-T3 alloy; (a1, a2) images at lower magnification; (a3, a4) higher magnification of the region above the particle in (a1, a2); (b) AA7475-T761 alloy; (b1, b2) images at lower magnification; (b3, b4) higher magnification of the region above the particle in (b1, b2). White arrows in (a3, b3) indicate highly porous oxide. Images were acquired in backscattered electron (BSE) and secondary electron (SE) modes at an accelerating voltage of 1.5 kV.

CRediT authorship contribution statement

João Victor de Sousa Araujo: Writing – original draft, Visualization, Validation, Methodology, Investigation, Formal analysis, Data curation, Conceptualization. **Jinghui Chen:** Investigation. **Isolda Costa:** Writing – review & editing, Supervision, Resources, Funding acquisition, Formal analysis. **Xiaorong Zhou:** Writing – review & editing, Visualization, Validation, Supervision, Resources, Project administration, Funding acquisition, Formal analysis, Data curation, Conceptualization.

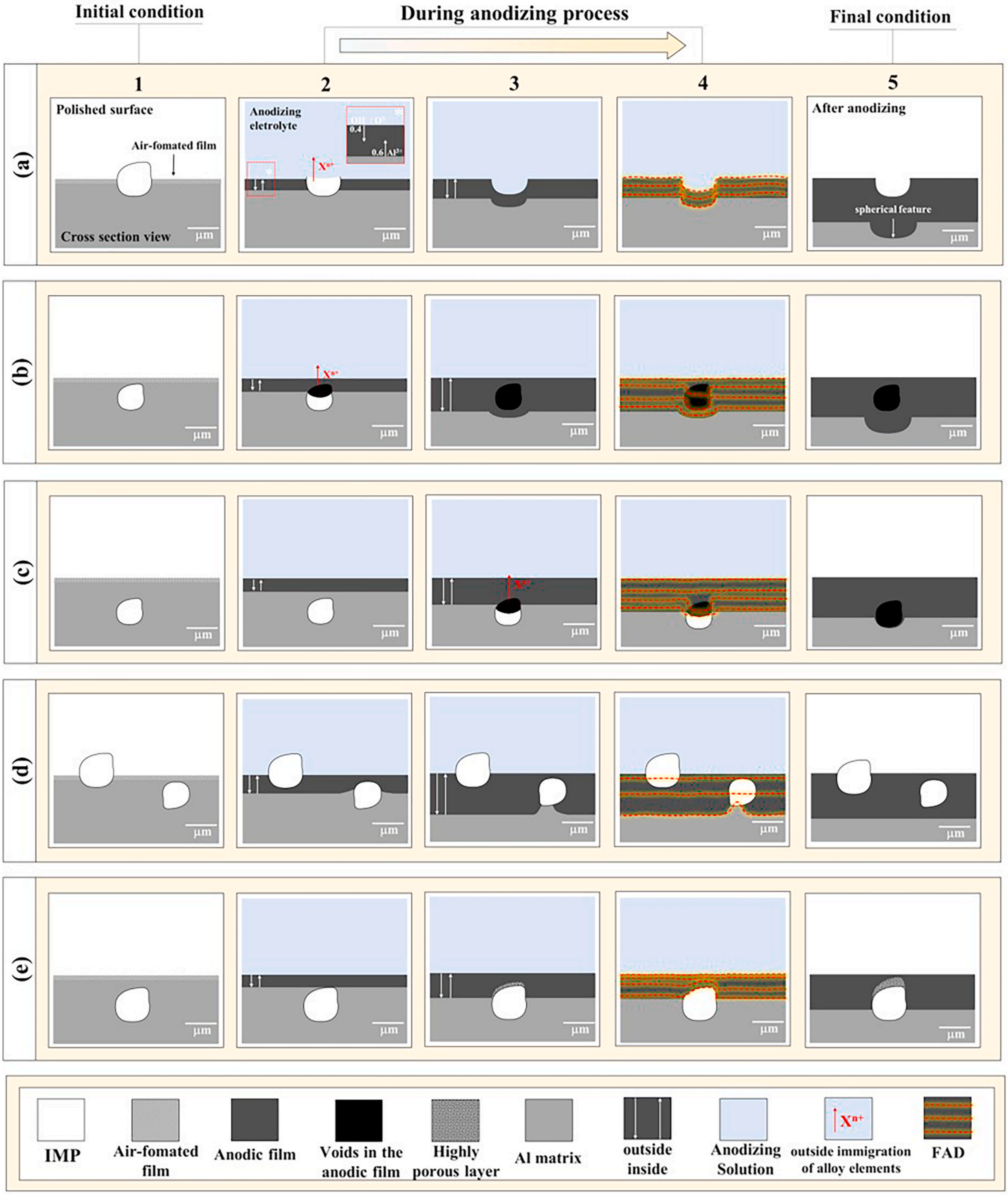

Fig. 11. – Schematic diagrams illustrating the anodizing behaviour of constituent intermetallic particles (IMPs) and their relation to the formation of various defect types during anodizing process of aluminium alloys: (a) high-copper-containing particle exposed at the surface; (b) high-copper-containing particle below the surface; (c) high-copper-containing particle exposed at the film/alloy interface; (d) particles containing inert elements; (e) Si-rich or low-copper-containing particle below the surface. The stages are as follows: (1) polished surface condition, showing the position of the IMP relative to the matrix; (2) initiation of the anodizing process and interaction between the particle and the electrolyte; (3) defect formation; (4) distribution of electric field lines based on the Field-Assisted Dissolution (FAD) theory; and (5) final location of the defect after anodizing. All diagrams assume a cross-sectional view of the IMP and defect formation.

Declaration of competing interest

The authors declare that they have no known competing financial interests or personal relationships that could have appeared to influence the work reported in this paper.

Acknowledgements

The authors gratefully acknowledge the financial support provided by FAPESP under grant numbers 2019/18388-1 and 2022/06935-0, awarded for the Ph.D. studies of João Victor de Sousa Araujo. Additionally, this work was supported by the UK EPSRC under grant EP/

S004963/1.

Data availability

Data will be made available on request.

References

[1] M. Curioni, M. Saenz De Miera, P. Skeldon, G.E. Thompson, J. Ferguson, Macroscopic and local filming behavior of AA2024 T3 aluminum alloy during anodizing in sulfuric acid electrolyte, J. Electrochem. Soc. 155 (2008) 387–395, https://doi.org/10.1149/1.2931522.

[2] M. Saenz de Miera, M. Curioni, P. Skeldon, G.E. Thompson, Modelling the anodizing behaviour of aluminium alloys in sulphuric acid through alloy analogues, Corros. Sci. 50 (2008) 3410–3415, https://doi.org/10.1016/j.corsci.2008.09.019.

[3] M. Saenz De Miera, M. Curioni, P. Skeldon, G.E. Thompson, Preferential anodic oxidation of second-phase constituents during anodising of AA2024-T3 and AA7075-T6 alloys, Surf. Interface Anal. 42 (2010) 241–246, https://doi.org/10.1002/sia.3191.

[4] M. Saenz de Miera, M. Curioni, P. Skeldon, G.E. Thompson, The behaviour of second phase particles during anodizing of aluminium alloys, Corros. Sci. 52 (2010) 2489–2497, https://doi.org/10.1016/j.corsci.2010.03.029.

[5] S.M. Moon, M. Sakairi, H. Takahashi, Behavior of second-phase particles in Al5052 alloy during anodizing in a sulfuric acid solution CSLM observation, J. Electrochem. Soc. 151 (2004) 399–405, https://doi.org/10.1149/1.1752933.

[6] S.-M. Moon, M. Sakairi, H. Takahashi, Application of CSLM to the surface morphological study of Al 5052 alloy anodized in sulfuric acid solution, J. Electrochem. Soc. 150 (2003) B473, https://doi.org/10.1149/1.1603248.

[7] B. Zhu, C. Zanella, Hardness and corrosion behaviour of anodised Al-Si produced by rheocasting, Mater. Des. 173 (2019) 107764, https://doi.org/10.1016/j.matdes.2019.107764.

[8] F. Zhang, J. Nilsson, J. Pan, In situ and operando AFM and EIS studies of anodization of Al 6060: influence of intermetallic particles, J. Electrochem. Soc. 163 (2016) C609–C618, https://doi.org/10.1149/2.0061610jes.

[9] B. Zhu, C. Zanella, Influence of Fe-rich intermetallics and their segregation on anodising properties of Al-Si-Mg rheocast alloys, Surf. Coat. Technol. 422 (2021) 127570, https://doi.org/10.1016/j.surfcoat.2021.127570.

[10] G. Scampone, G. Timelli, Anodizing Al–Si foundry alloys: a critical review, Adv. Eng. Mater. 24 (2022) 2101480, https://doi.org/10.1002/adem.202101480.

[11] J.V. de Sousa Araujo, M. Xavier Milagre, R. Emil Klumpp, V. Hugo Ayusso, U. Donatus, I. Costa, TSA anodising voltage effects on the near-surface coarse intermetallic particles in the AA2024-T3 and AA2198-T8 alloys, Corrosion Eng. Sci. Technol. 57 (2022) 380–396, https://doi.org/10.1080/1478422X.2022.2071666.

[12] Y. Ma, X. Zhou, G.E. Thompson, M. Curioni, X. Zhong, E. Koroleva, P. Skeldon, P. Thomson, M. Fowles, Discontinuities in the porous anodic film formed on AA2099-T8 aluminium alloy, Corros. Sci. 53 (2011) 4141–4151, https://doi.org/10.1016/j.corsci.2011.08.023.

[13] Y. Ma, X. Chen, X. Zhou, Y. Yi, Y. Liao, W. Huang, Microstructural origin of localized corrosion in anodized AA2099-T8 aluminium–lithium alloy, Surf. Interface Anal. 48 (2016) 739–744, https://doi.org/10.1002/sia.5856.

[14] M. Bononi, M. Conte, R. Giovanardi, A. Bozza, Hard anodizing of AA2099-T8 aluminum lithium copper alloy: influence of electric cycle, electrolytic bath composition and temperature, Surf. Coat. Technol. 325 (2017) 627–635, https://doi.org/10.1016/j.surfcoat.2017.07.028.

[15] H. Wu, Y. Ma, W. Huang, X. Zhou, K. Li, Y. Liao, Z. Wang, Z. Liang, L. Liu, Effect of iron-containing intermetallic particles on film structure and corrosion resistance of anodized AA2099 alloy, J. Electrochem. Soc. 165 (2018) C573–C581, https://doi.org/10.1149/2.1361809jes.

[16] Y. Ma, H. Wu, X. Zhou, K. Li, Y. Liao, Z. Liang, L. Liu, Corrosion behavior of anodized Al-Cu-Li alloy: the role of intermetallic particle-introduced film defects, Corros. Sci. 158 (2019) 108110, https://doi.org/10.1016/j.corsci.2019.108110.

[17] D. Veys-Renaux, N. Chahboun, E. Rocca, Anodizing of multiphase aluminium alloys in sulfuric acid: in-situ electrochemical behaviour and oxide properties, Electrochim. Acta 211 (2016) 1056–1065, https://doi.org/10.1016/j.electacta.2016.06.131.

[18] D. Nickel, D. Dietrich, R. Morgenstern, I. Scharf, H. Podlesak, T. Lampke, Anodisation of aluminium alloys by micro-capillary technique as a tool for reliable, cost-efficient, and quick process parameter determination, Adv. Mater. Sci. Eng. 2016 (2016) 1–12, https://doi.org/10.1155/2016/1374897.

[19] J.V. Araujo, M. Xavier Milagre, A.D. Gabbardo, R.E. Klumpp, I. Costa, The effect of tartaric-sulfuric acid (TSA) anodizing on the corrosion resistance of the AA7475-T761, in: ECS Meet. Abstr. MA2022-02, 2022, https://doi.org/10.1149/MA2022-02142475mtgabs, 2475–2475.

[20] J.M. Runge, Trace elements and their impact on surface finishing characteristics of aluminum extrusions, in: Proc. ET, 2012. Miami.

[21] J.M. Runge, T. Hossain, Interfacial Phenomena in 7000 Series Alloys and their Impact on the Anodic Oxide, Elsevier Ltd., 2015, https://doi.org/10.1016/j.matpr.2015.10.096.

[22] Jude Mary Runge, Anodizing complex 7000 series, Light Met. Age 74 (2016) 52–56.

[23] Y. Sen Huang, T.S. Shih, J.H. Chou, Electrochemical behavior of anodized AA7075-T73 alloys as affected by the matrix structure, Appl. Surf. Sci. 283 (2013) 249–257, https://doi.org/10.1016/j.apsusc.2013.06.094.

[24] J.V. de Sousa Araujo, M.X. Milagre, X. Zhou, I. Costa, An assessment of pitting corrosion in anodized aluminum alloys: it might not be what it seems, Mater. Corros. 75 (2024) 599–613, https://doi.org/10.1002/maco.202313977.

[25] J.V. de S. Araujo, M. Milagre, I. Costa, A historical, statistical and electrochemical approach on the effect of microstructure in the anodizing of Al alloys: a review, Crit. Rev. Solid State Mater. Sci. 49 (2023) 521–581, https://doi.org/10.1080/10408436.2023.2230250.

[26] N.E. Prasad, R.J.H. Wanhill, in: Aerospace Materials and Material Technology, vol. 1, 2016.

[27] K. Shimizu, G.M. Brown, K. Kobayashi, P. Skeldon, G.E. Thompson, G.C. Wood, Ultramicrotomy – a route towards the enhanced understanding of the corrosion and filming behaviour of aluminium and its alloys, Corros. Sci. 40 (1998) 1049–1072, https://doi.org/10.1016/S0010-938X(98)00006-7.

[28] R.D. Guminski, P.G. Sheasby, H.J. Lamb, Reaction rates of second-phase constituents in aluminium during etching, brightening and oxalic acid anodizing processes, Trans. IMF 46 (1968) 44–48, https://doi.org/10.1080/00202967.1968.11870048.

[29] H. Habazaki, K. Shimizu, P. Skeldon, G.E. Thompson, G.C. Wood, X. Zhou, Effects of alloying elements in anodizing of aluminium, Trans. Inst. Met. Finish. 75 (1997) 18–23, https://doi.org/10.1080/00202967.1997.11871137.

[30] H.A. Elkilany, M.A. Shoeib, O.E. Abdel-Salam, Influence of hard anodizing on the mechanical and corrosion properties of different aluminum alloys, Metallogr. Microstruct. Anal. 8 (2019) 861–870, https://doi.org/10.1007/s13632-019-00594-5.

[31] Y. Ma, X. Zhou, J. Wang, G.E. Thompson, W. Huang, J.O. Nilsson, M. Gustavsson, A. Crispin, Discoloration of anodized AA6063 aluminum alloy, J. Electrochem. Soc. 161 (2014), https://doi.org/10.1149/2.065406jes.

[32] J.S. Pinheiro, H.R.P. Cardoso, K.R. Pereira, C. Radtke, S. Kunst, C.T. Oliveira, J. Zoppas Ferreira, Chromium/nickel-free conversion coating as cold post-treatment to anodized AA2024-T3 for corrosion resistance increase, Surf. Coat. Technol. 480 (2024) 130566, https://doi.org/10.1016/j.surfcoat.2024.130566.

[33] M. Hou, C. Pan, M. Wang, D.-H. Xia, Z. Qin, W. Hu, Improving the cavitation corrosion resistance of 6061 aluminum alloy by anodizing, Electrochim. Acta 503 (2024) 144890, https://doi.org/10.1016/j.electacta.2024.144890.

[34] J.V. de S. Araujo, J. Chen, I. Costa, X. Zhou, Localized corrosion in anodized aluminium alloys: the role of constituent particle-induced defects in anodic films, Corros. Sci. (2025) 112961, https://doi.org/10.1016/J.CORSCI.2025.112961.

[35] J.R. Davis, Aluminium and Aluminium Alloys, ASM International, Materials Park, 1993.

[36] E. Kock, C. Dr Gerlach, M. Dr Beneke, Anodizing Process for Aluminum Materials, 2004. DE10361888B3.

[37] K. Shimizu, T. Mitani, in: Application Example 12: Cross-Sectional Examination of an Anodized Aluminum Alloy for Aerospace Application, 2010, pp. 37–38, https://doi.org/10.1007/978-3-642-03160-1_13.

[38] J. Long, A. Borissova, A.D. Wilson, J.C. Avelar-Batista Wilson, Sample preparation of anodised aluminium oxide coatings for scanning electron microscopy, Micron 101 (2017) 87–94, https://doi.org/10.1016/j.micron.2017.06.010.

[39] J.V. de Sousa Araujo, A.F. Santos Bugarin, U. Donatus, C.S.C. Machado, F. M. Queiroz, M. Terada, A. Astarita, I. Costa, Thermomechanical treatment and corrosion resistance correlation in the AA2198 al–cu–li alloy, Corrosion Eng. Sci. Technol. 54 (2019) 575–586, https://doi.org/10.1080/1478422X.2019.1637077.

[40] J.V. de Sousa Araujo, I. Costa, X. Zhou, Comparison of constituent intermetallic particles in different aluminium alloys, Metallogr. Microstruct. Anal. (2025), https://doi.org/10.1007/s13632-025-01170-w.

[41] Y. Ma, X. Zhou, G.E. Thompson, M. Curioni, X. Zhong, E. Koroleva, P. Skeldon, P. Thomson, M. Fowles, Discontinuities in the porous anodic film formed on AA2099-T8 aluminium alloy, Corros. Sci. 53 (2011) 4141–4151, https://doi.org/10.1016/j.corsci.2011.08.023.

[42] S.P.A. Alenia Aeronautica, Anodizing Process, with Low Environmental Impact, for a Workpiece of Aluminium or Aluminium Alloys, European Patent Application EP 1233084 A2.

[43] L. Zhang, G.E. Thompson, M. Curioni, P. Skeldon, Anodizing of aluminum in sulfuric Acid/Boric acid mixed electrolyte, J. Electrochem. Soc. 160 (2013) C179–C184, https://doi.org/10.1149/2.032306jes.

[44] H. Wu, Y. Ma, W. Huang, X. Zhou, K. Li, Y. Liao, Z. Wang, Z. Liang, L. Liu, Effect of iron-containing intermetallic particles on film structure and corrosion resistance of anodized AA2099 alloy, J. Electrochem. Soc. 165 (2018) C573–C581, https://doi.org/10.1149/2.1361809jes.

[45] K. Shimizu, T. Mitani, in: Application Example 12: Cross-Sectional Examination of an Anodized Aluminum Alloy for Aerospace Application, 2010, pp. 37–38, https://doi.org/10.1007/978-3-642-03160-1_13.

[46] K. Kobayashi, K. Shimizu, Y. Tsuda, Structure of porous anodic films formed on Al-Si alloys, J. Jpn. Inst. Light Met. 37 (1987) 807–810, https://doi.org/10.2464/jilm.37.807.

[47] G.E. Thompson, H. Habazaki, K. Shimizu, M. Sakairi, G.C. Wood, Anodizing of aluminium alloys, Aircraft Eng. Aero. Technol. 71 (1999) 228–238.

[48] D. Nickel, D. Dietrich, R. Morgenstern, I. Scharf, H. Podlesak, T. Lampke, Anodisation of aluminium alloys by micro-capillary technique as a tool for reliable, cost-efficient, and quick process parameter determination, Adv. Mater. Sci. Eng. 2016 (2016) 1–12, https://doi.org/10.1155/2016/1374897.

[49] K. Shimizu, K. Kobayashi, G.E. Thompson, P. Skeldon, G.C. Wood, The influence of θ' precipitates on the anodizing behaviour of binary Al-Cu alloys, Corros. Sci. 39 (1997) 281–284, https://doi.org/10.1016/S0010-938X(97)83347-1.

[50] E. Palibroda, A. Lupsan, S. Pruneanu, M. Savos, Aluminium porous oxide growth. On the electric conductivity of the barrier layer, Thin Solid Films 256 (1995) 101–105, https://doi.org/10.1016/0040-6090(94)06293-5.

[51] G.E. Thompson, G.C. Wood, Porous anodic film formation on aluminium, Nature 290 (1981) 230–232, https://doi.org/10.1038/290230a0.

[52] J.P. O'Sullivan, G.C. Wood, The morphology and mechanism of formation of porous anodic films on aluminium, Proc. R. Soc. Lond. A 317 (1970) 511–543, https://doi.org/10.1098/rspa.1970.0129.

[53] M. Saenz De Miera, M. Curioni, P. Skeldon, G.E. Thompson, Preferential anodic oxidation of second-phase constituents during anodising of AA2024-T3 and AA7075-T6 alloys, Surf. Interface Anal. 42 (2010) 241–246, https://doi.org/10.1002/sia.3191.

[54] L. Iglesias-Rubianes, S.J. Garcia-Vergara, P. Skeldon, G.E. Thompson, J. Ferguson, M. Beneke, Cyclic oxidation processes during anodizing of Al-Cu alloys, Electrochim. Acta 52 (2007) 7148–7157, https://doi.org/10.1016/j.electacta.2007.05.052.

[55] G.C. Wood, J.P. O'Sullivan, The anodizing of aluminium in sulphate solutions, Electrochim. Acta 15 (1970) 1865–1876, https://doi.org/10.1016/0013-4686(70)85024-1.

[56] M. Shahid, Mechanism of film growth during anodizing of Al-alloy-8090/SiC metal matrix composite in sulphuric acid electrolyte, J. Mater. Sci. 32 (1997) 3775–3781, https://doi.org/10.1023/A:1018623623116.

[57] H. Habazaki, X. Zhou, K. Shimizu, P. Skeldon, G.E. Thompson, G.C. Wood, Mobility of copper ions in anodic alumina films, Electrochim. Acta 42 (1997) 2627–2635, https://doi.org/10.1016/S0013-4686(96)00454-9.

[58] Z. Jin, C. Cai, T. Hashimoto, Y. Yuan, D.H. Kang, J. Hunter, X. Zhou, The behaviour of iron-containing intermetallic particles in aluminium alloys in alkaline solution, Corros. Sci. (2020), https://doi.org/10.1016/j.corsci.2020.109134.

[59] V.K. P, M. V, M. G, E. S, Developing digital twin design for enhanced productivity of an automated anodizing industry and process prediction using hybrid deep neural network, Eng. Appl. Artif. Intell. 122 (2023) 106086, https://doi.org/10.1016/j.engappai.2023.106086.

[60] S.V. Kalinin, D. Mukherjee, K. Roccapriore, B.J. Blaiszik, A. Ghosh, M.A. Ziatdinov, A. Al-Najjar, C. Doty, S. Akers, N.S. Rao, J.C. Agar, S.R. Spurgeon, Machine learning for automated experimentation in scanning transmission electron microscopy, npj Comput. Mater. 9 (2023) 227, https://doi.org/10.1038/s41524-023-01142-0.

[61] A. Chowdhury, E. Kautz, B. Yener, D. Lewis, Image driven machine learning methods for microstructure recognition, Comput. Mater. Sci. 123 (2016) 176–187, https://doi.org/10.1016/j.commatsci.2016.05.034.